Reconfigurable Broadband Metasurface with Switchable Functionalities in the Visible Range

MD. EHSANUL KARIM[1,2], AND SAJID MUHAIMIN CHOUDHURY[1,*]

[1] *Department of Electrical and Electronic Engineering, Bangladesh University of Engineering and Technology, Dhaka- 1205, Bangladesh*
[2] *Department of Electrical and Electronic Engineering, BRAC University, Dhaka- 1212, Bangladesh*
[*] *Corresponding Author: sajid@eee.buet.ac.bd*

Abstract: In this article, we propose a broadband reconfigurable multifunctional meta-structure for the first time in the visible range. This device can be reconfigured between an achromatic metalens and a broadband absorber by switching the state of the phase change material (VO_2). Our designed VO_2 based novel multistage meta-atoms helped us overcome the inherent limitation of small optical contrast between PCM states in the visible regime, which hinders the realization of reconfigurable multifunctional devices in this band. We have used the finite-difference time-domain (FDTD) technique to characterize the designed multifunctional device. The structure showed a maximum switching ratio of 21.1dB between the on and off states, the highest among previously reported broadband metalens-absorber systems in any design band. A small focal length shift within ±5% in the on state within the 678nm to 795nm band verifies the achromatic focusing characteristics. Our device proves the feasibility of reconfigurable metasurfaces with switchable functionalities in the visible band and has the prospects to bring about a revolution in next-generation integrated photonic platforms.

© 2023 Optica Publishing Group under the terms of the Optica Open Access Publishing Agreement

1. Introduction

Metasurfaces, the two-dimensional analog of metamaterials [1], have attracted immense interest from the scientific community over the last two decades for their unique capability of controlling and manipulating light. Based on this distinctive feature of metasurfaces, several meta-devices like metalens [2, 3], absorber [4, 5], invisible cloak [6], beam steering [7], holography [8, 9], nano-lasers [10], color displays [11] have been developed. But with the ever-increasing demand for miniaturization and integration in complex systems, there has been a growing interest in combining several of these functionalities into a single metasurface.

Several works involving multifunctional metasurfaces have been reported in recent years for the IR and microwave regime [12–17]. These devices utilize phase change materials (PCM), graphene, varactor diode, PIN diode, and micro-electromechanical system (MEMS) for switching between different functionalities. Among these approaches PCMs like vanadium dioxide(VO_2), $Ge_2Sb_2Te_5$(GST), $Ge_2Sb_2Se_4Te_1$(GSST) provide the most viable path to commercialization of reconfigurable, multifunctional meta-devices due to their repeatable, fast, and reversible switching, notable contrast in optical properties of the two states, and chemical stability [18–20]. VO_2 has emerged as a lower power-consuming alternative to other PCMs [21]. Thermal, optical, or electrical stimuli can cause VO_2 to switch from an insulating to a metallic state [22]. This ultrafast phase transition with a picosecond timescale [23] at a relatively low temperature of 68^{o}C [24] and significant dissimilarity in optical properties of the two states [25] makes VO_2 a suitable candidate for broadband switchable meta-device design in the IR and microwave range [12, 26, 27]. But the relatively small variation in refractive index for the two states of VO_2 and PCMs in general in the visible regime, however, makes broadband switchable characteristics difficult to realize. There have been reports of metasurfaces with switchable functionality in the visible range [28–32]. But the switching is based on the incident light polarization, and

these devices offer very similar functionalities. To the best of our knowledge, a reconfigurable metasurface with diversified functionalities in the visible spectrum has not yet been reported.

In this paper, we propose a broadband reconfigurable metasurface that can be switched between an achromatic metalens and a near-perfect broadband absorber in the visible portion of the EM spectrum by exciting phase transition of VO_2. For this, we have designed a broadband switchable absorber in the visible range as the unit cell of this dual-functional device. The multistage structure of the meta-atom allowed us to enhance the additional Fabry-Perot cavity mode induced in the metallic state of VO_2 due to the small contrast between the two states. The cell has near-perfect absorption in the metallic phase and good transmission characteristics in the insulating phase of VO_2 in the 689.3-774.6nm band. This is an unprecedented absorption characteristic in the visible range compared to absorption peak tuning demonstrated in previous PCM-based absorber structures [33–36]. We utilize this broadband switchable absorber as a constituent meta-atom for our multifunctional meta-device, which acts as an achromatic metalens and a broadband absorber in the visible range for the insulating (on) and metallic (off) state of VO2, respectively. This reconfigurable multifunctionality of our designed metasurface is demonstrated by the normalized focal length shift of less than ±5% in the on state and a maximum contrast of 21.1dB between the on and off states in the 678-795nm wavelength range. This broadband metalens-absorber system has the highest switching ratio among those previously reported for any design band [32, 37–39]. This kind of dual-functional meta-device may find wide range of applications in smart bioimaging due to its dose-sensitive, ultrafast switching capability. This work will open new horizons for miniaturized integrated photonic devices in visible range by paving the way for reconfigurable multifunctional devices.

2. Unit cell structural layout

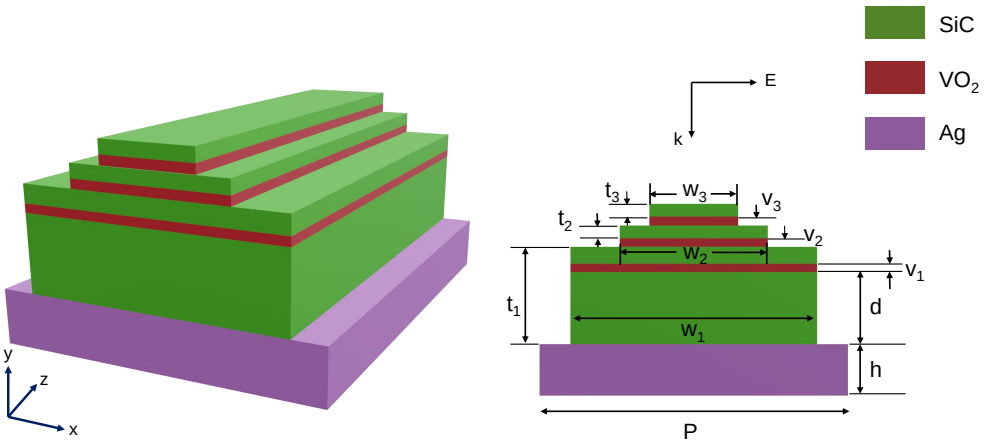

Fig. 1. The **(a)** 3D schematic and **(b)** x-y plane cross-sectional view of our proposed broadband switchable absorber unit with different structural parameters marked. P is the periodicity of the unit cell, while the thickness of the substrate is marked as h. The cavity length, width, and VO_2 layer thickness of the ith stage are represented by t_i, w_i, and v_i respectively with i=1,2, and 3. d marks the position of the VO_2 layer above the substrate in the lowest stage.

Our reconfigurable multifunctional metasurface is designed based on switchable absorber meta-atoms. Fig. 1 illustrates the structural layout of the designed meta-unit. The unit cell is constructed from three stages, each of which consists of a thin VO_2 sheet placed between two Silicon Carbide (SiC) layers. A thick layer of Silver is used as the substrate of this structure to minimize the transmission through the substrate. The substrate thickness (h) has been chosen accordingly. The previous works in Ref. [40–43] show the feasibility of the practical realization of such a structure. However, the hands-on fabrication of the proposed absorber cell is beyond the extent of this work.

We have numerically investigated switchable absorption characteristics of the meta-atom by FDTD method using the commercial software Lumerical FDTD Solutions. In the simulation environment, an x-polarized plane wave source propagating along the negative y direction illuminates the unit cell as depicted in Fig. 1(b) by the directions of electric field vector (E) and propagation vector (k) respectively. The structural parameters of the unit cell shown in Fig. 1(b) have been varied in the FDTD simulation to achieve the optimum bandwidth and modulation depth of the absorption characteristics. The reflection (R) from a single cell was calculated by a 2d frequency domain power monitor. Since the transmission through the thick Ag layer is negligible, the absorption of the structure is given by $A = 1 - R$. The simulation setup contains periodic and perfectly matched layer (PML) boundary conditions in the longitudinal (x) and transverse (y) directions, respectively. We have used the experimentally obtained optical properties of the insulator and metallic phases of VO_2 reported by Dicken et al. [25] in our numerical model. For refractive indices of Ag and SiC, the Palik model [44] and Ref. [45] has been used, respectively.

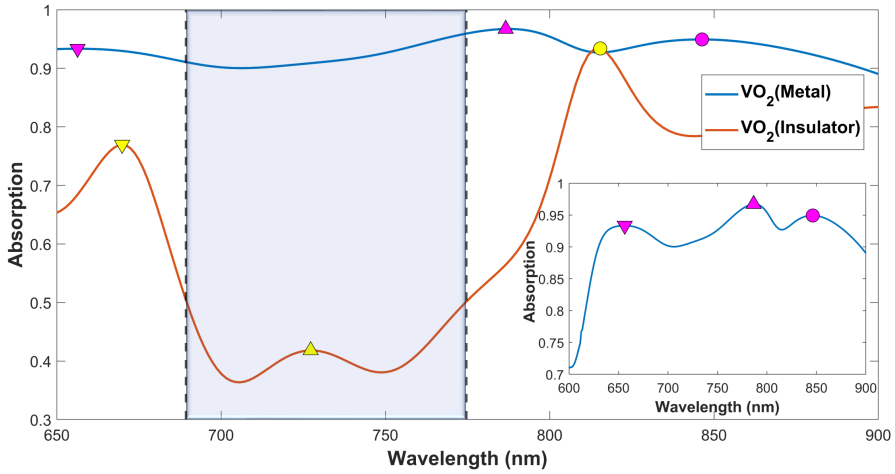

Fig. 2. The absorption spectra of the unit cell for the metallic and insulating phases of the VO_2 layer with P=600nm, h=100nm, w_1=480nm, w_2=288nm, w_3=172.8nm, d=140nm, v_1=v_2=v_3=17nm, and t_1=190nm, t_2=t_3=24.75nm. The shaded region represents the switchable region with absorption greater than 90% for the metallic state and less than 50% for the insulating state. The inset gives an enlarged view of the absorption curve at the off state (metallic phase of VO_2). The symbols $\triangledown$, $\triangle$, and $\circ$ represent the positions of Modes 1, 2, and 3, respectively. Mode 2 in the insulating state is extremely weak and will not be further investigated.

3. Absorption characteristics of the unit cell

The contrast in absorption characteristic of our designed unit cell at the on (VO_2 in the insulating phase) and off (VO_2 in the metallic phase) states, is depicted in Fig. 2. The absorption spectrum for the insulating phase shows two narrow peaks at 669nm (Mode 1) and 815nm (Mode 3). In the metallic phase, another peak becomes prominent at 786nm (Mode 2) as marked in Fig. 2. The emergence of an additional peak in the metallic state results in a broadband absorption spectrum under external stimulus. The blue-shaded region in Fig. 2 from 689.3nm to 774.6nm represents the region with switchable absorption characteristics. This 85.3nm band shows broadband 'on-off' switching characteristics between the two states of the PCM in the real sense, compared to simple absorption peak shifting in previously reported works for the visible regime [33–36].

To further investigate the origin of this broadband switchable absorption characteristics, we have simulated the spatial electric field profiles of the unit cells in both the on (insulting) and off (metallic) states, as shown in Fig. 3. For the field profiles, we have used the standard structure as in Fig. 2. To validate our observations from the field distribution, we have also studied the impact of different structural parameters on the absorption spectrum depicted in Fig. 4 and 5. When varying one of the parameters, the others have been kept constant at their standard values.

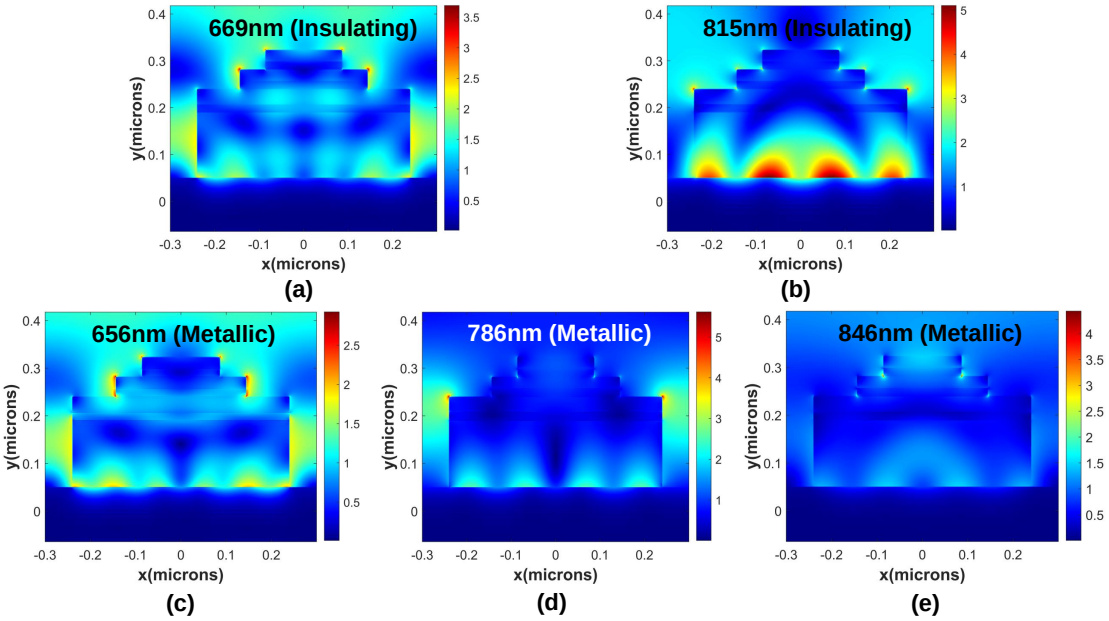

Fig. 3. The spatial electrical field distribution of the unit cell in the x-y plane for (**a-b**) Mode 1 and 2 in the insulating state and (**c-e**) Mode 1,2, and 3 in the metallic phase of VO_2. The electric field values have been normalized by the incident field amplitude.

For Mode 1, the electric field is concentrated around the Ag substrate and the SiC spacer for the insulating state (Fig. 3(a)), indicating the contribution of a Fabry-Perot (FP) cavity mode. The similarity of SiC and VO_2 refractive indices at room temperature means that a continuous cavity is formed between the substrate and the upper stage SiC-air interface with a cavity length of $t_1 + t_2 + t_3$. This FP cavity length is directly proportional to the resonant wavelength [46], which causes the redshift of Mode 1 position with increasing t_1, t_2, and t_3 in Fig. 4(a-c) respectively. Also, the insensitivity of Mode 1 on lower VO_2 layer position (d) (Fig. 5(a)) further indicates the formation of a continuous cavity in the insulating state. The red shift of this resonant wavelength with cavity width (w_1) in Fig. 5(c) is also consistent with previously reported observations [47,48]

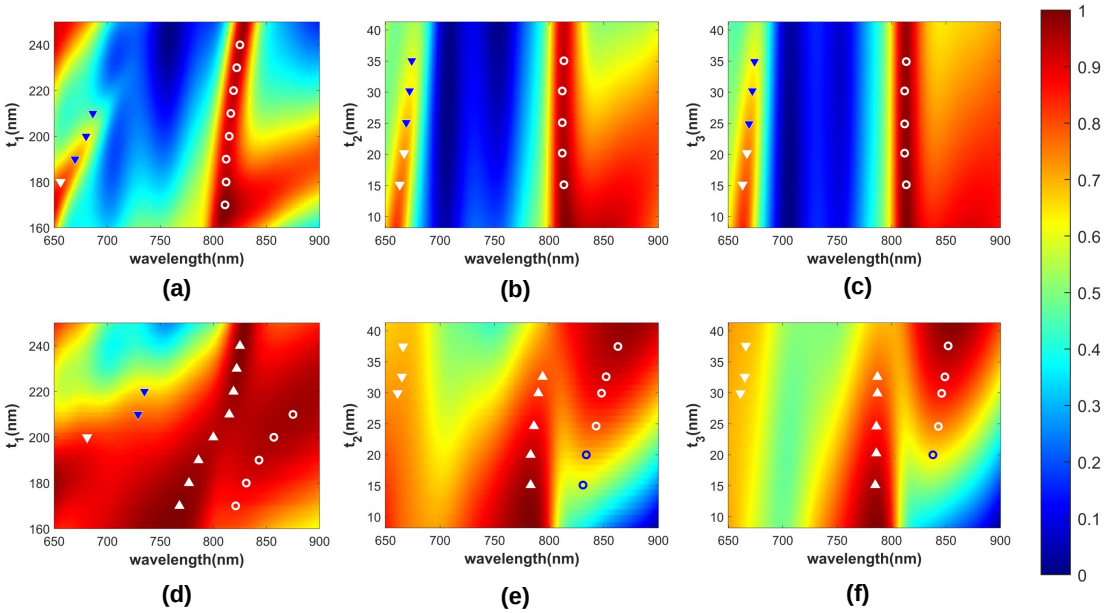

Fig. 4. Absorption color maps as a function of wavelength and t_1, t_2, t_3 for (**a-c**) insulating and (**d-f**) metallic VO_2, respectively. The symbols $\triangledown$, $\triangle$, and $\circ$ represent the shifting of Modes 1, 2, and 3 resonant peaks, respectively.

for FP resonance. The metallic state shows strong field concentration around the VO_2 layers and the corresponding spacer (SiC) (Fig. 3(c)), indicating FP cavity modes formed between the metallic VO_2 and SiC-air interfaces. Apart from a strong dependence on t_1, t_2, and t_3 as depicted in Fig. 4(d-f), the absorption peak shows a strong blueshift with increasing d as well (Fig. 5(d)). This is due to the dependence of the cavity length $(t_1 - d)$ on d, unlike the insulating phase with a continuous cavity between Ag and SiC. This resonant peak also shows a strong dependency on w_1, as shown in Fig. 5(f), similar to that for the insulating state.

For Mode 2 in the metallic state, the absorption peak shows a strong dependency on t_1 and d in Fig. 4(d) and Fig. 5(d) respectively, indicating the contribution from the lower FP cavity with a length of $(t_1 - d)$. The resonant wavelength also shows a weak redshift with increasing t_2 and t_3 (Fig. 4(e-f)). The increase of this peak wavelength with increasing w_1 in Fig. 5(f) is also consistent with our previous observations. The field distribution at this wavelength (Fig. 3(d)), as well as strong dependency on the period(P) in Fig. 5(e), shows the impact of adjacent cell coupling on this absorption peak. As P increases, the greater separation between the neighboring cells causes a decrease in the resonant energy and hence causes the redshift.

The field distribution of Mode 3 for insulating VO_2 in Fig. 3(b) shows a strong concentration between Ag and the top SiC-air interface. This indicates the presence of an FP mode, which is further validated by the redshift of the peak wavelength with increasing t_1 (Fig. 4(a)). The resonance position moves towards higher wavelengths as the cavity width (w_1) increases (Fig. 5(c)). The redshift with increasing P in Fig. 5(b) indicates the contribution of unit cell coupling to this absorption peak. For the metallic state of VO_2 at higher temperatures, the field distribution(Fig. 3(e)) is very similar to that for Mode 1(Fig. 3(c)). The visual dissimilarity is due to the unexpectedly high field concentration around one of the VO_2 edges which shifts the color bar scale upwards. As a result, the position of this peak shows very similar dependency on t_1, t_2, t_3, and w_1 as for Mode 1. However, there is a weak dependency on d (Fig. 5(d)), which

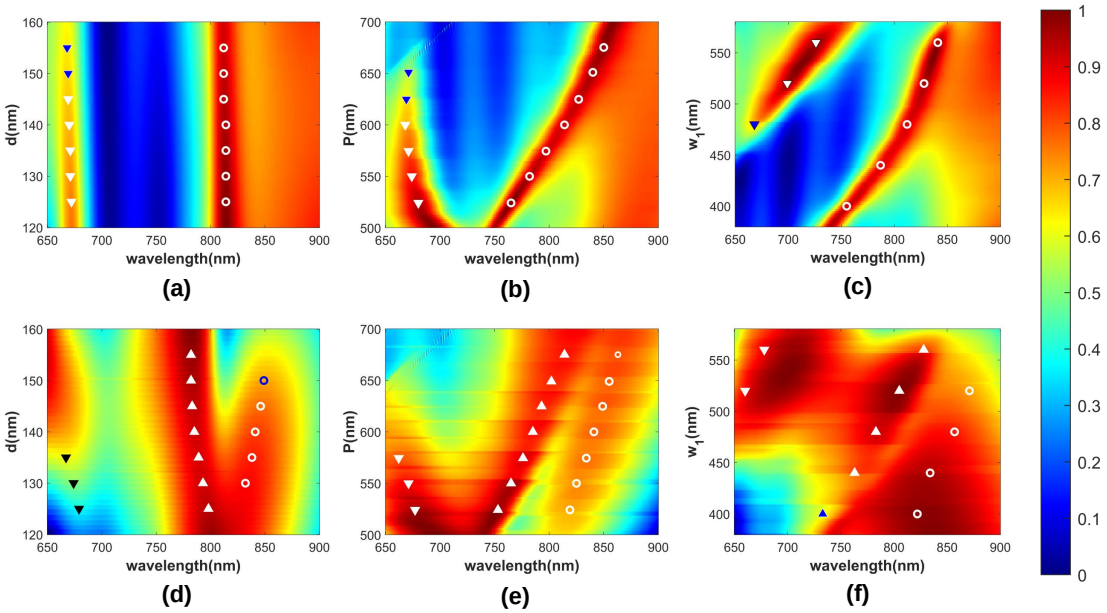

Fig. 5. Absorption color maps as a function of wavelength and d, P, and w_1 for (**a-c**) insulating and (**d-f**) metallic VO_2, respectively. The symbols $\triangledown$, $\triangle$, and $\circ$ represent the absorption peak variation paths for Modes 1, 2, and 3, respectively.

is due to the relatively weak FP cavity mode contribution from the lower cavity. The strong dependency of the resonant wavelength on the period (P) in Fig. 5(e) validates the presence of unit cell coupling indicated in the spatial field distribution.

4. Design of the switchable broadband metasurfcae

We have utilized the switchable broadband absorber proposed in Section 2 as a unit cell to design our broadband meta-device reconfigurable between an achromatic metalens and a broadband near-perfect absorber. The design methodology for broadband achromatic metalens has been previously reported [49, 50]. Apart from that, we have selected the unit cells to maintain their switching bandwidth as defined in Section 3. Addressing these requirements in all the points on the metalens ensures that the metasurface can be switched between its on(achromatic metalens) and off(broadband absorber) states.

The required relative phase $\phi(r, \omega)$ at any point r on the metalens with respect to its center for a focal length of f is given by [51]

$$\phi(r, \omega) = -\frac{\omega}{c}(\sqrt{r^2 + f^2} - f) \tag{1}$$

where c and ω represent the speed and angular frequency of the incident light respectively. This equation should be satisfied at the complete frequency range of the design to achieve achromatic focusing. Eq. 1 can be expanded about a reference frequency of ω_r using the Taylor series theorem

$$\phi(r, \omega) = \phi(r, \omega_r) + \frac{\partial \phi(r, \omega)}{\partial \omega}\bigg|_{\omega=\omega_r} (\omega - \omega_r) + \frac{\partial^2 \phi(r, \omega)}{2\partial^2 \omega}\bigg|_{\omega=\omega_r} (\omega - \omega_r)^2 + \ldots \tag{2}$$

The first term in Eq. 2 is the one that is satisfied in single wavelength metalens. The first ($\frac{\partial\phi(x,\omega)}{\partial\omega}\Big|_{\omega=\omega_r}$) and second order derivative terms($\frac{\partial^2\phi(x,\omega)}{\partial^2\omega}\Big|_{\omega=\omega_r}$) around ω_r in the equation, are called relative group delay and group delay dispersion respectively [50]. For achromatic focusing with a bandwidth of $\Delta\omega$ around ω_r, these terms, along with the other higher order derivatives, must be satisfied at each point on the metalens. For our switchable metasurface, another requirement is maintaining the switchable absorption characteristic at each point of the lens. We define this switchable band as the region with less than 60% absorption in the on state and greater than 90% absorption in the off state.

To satisfy these constraints, we have constructed a meta-atom library by simulating our unit cell absorber structure reported in Section 2 with different structural parameters. For this, the cavity lengths (t_1,t_2,t_3), widths (t_1,t_2,t_3), and position of VO_2 above the substrate (d) in Fig. 1(b) have been varied. The thicknesses of the VO_2 layers (v_1, v_2, v_3) have also been tuned and have been kept equal to each other for all the meta-atoms considered. Three representative meta-atom structures and their corresponding phase spectra are illustrated in Fig. 6(a). The linear shaded region of the spectrum, from 685.6nm to 774nm, is considered our design band for this

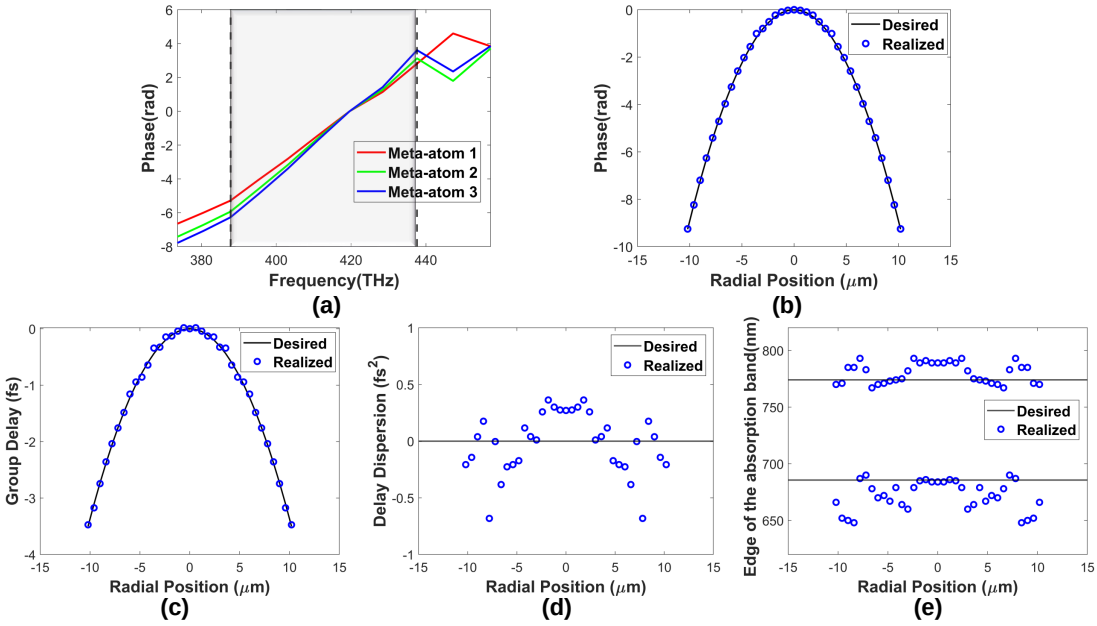

Fig. 6. **(a)** Phase spectra of three representative unit cells from our meta-atom library. The shaded area (685.6nm to 774nm) marks the design band (linear phase region). The structural parameters (d, w_1, w_2, w_3, t_1, t_2, t_3, v_1 =v_2= v_3) for the Meta-atom 1 to 3 are (140, 485, 242.5, 145.5, 190, 22.75, 24.4, 17.5), (145, 461, 189, 152, 186, 20, 20, 16), and (140, 490, 416.5, 73.5, 190, 24.75, 24.5, 17) respectively in nanometer units. Required and realized **(b)** relative phase, **(c)** relative group delay, **(d)** relative group delay dispersion, and **(e)** switchable absorption band spread as a function of radial position on the metasurface. The desired values in (b-d) are for an achromatic metalens designed for a focal length (f) of 49μm with a radius of 10.2μm. The requirement for the switchable band in (e) means that the upper and lower limits of the realized unit cell band should be above and below the reference lines respectively. The realized values in (b-e) represent the response of the appropriate unit cell chosen from our meta-atom library for that position.

broadband metalens. Fig. 6(b-d) shows the required values of relative phase, group delay, and delay dispersion on each point of the metasurface. These requirements have been satisfied for the on state(insulating VO_2) only since in the off state(metallic VO_2), the device will work as a nearly perfect absorber. This is ensured by maintaining a less than 60% absorption for the on-state and greater than 90% absorption in the off-state throughout the design bandwidth. Fig. 6(e) shows the realized upper and lower absorption band limits. The two lines in the figure labeled "required" represent the upper and lower boundaries of the linear region marked in Fig.6(a). The relative phase, delay, and switchable bandwidth requirements have been closely satisfied in all the points by choosing appropriate meta-atom cells from our constructed library, as shown in Fig. 6(b,c,e). However, due to the uniformity of the basic structure throughout the device and the constraint of aligning the absorption band with the linear phase band, the relative group delay dispersion requirement could not be satisfied perfectly in all the points (Fig. 6(d)). Higher order derivative terms in Eq. 2 have not been considered in our design as the relative values of these terms are negligible for all our selected meta-atoms.

5. Characterization of the reconfigurable broadband meta-device

Our dual-functional metasurface has been constructed by placing the unit cells reported in Section 4 at their respective positions, as schematically shown in Fig. 7(a). To evaluate the broadband switching and focusing characteristics, we simulated the structure by the FDTD technique in the commercial software, Lumerical FDTD Solutions. For this, the structure was illuminated with an x-polarized source propagating in the -y direction. PML boundary conditions were used in both the x and y directions, a typical setting used in previous works [52].

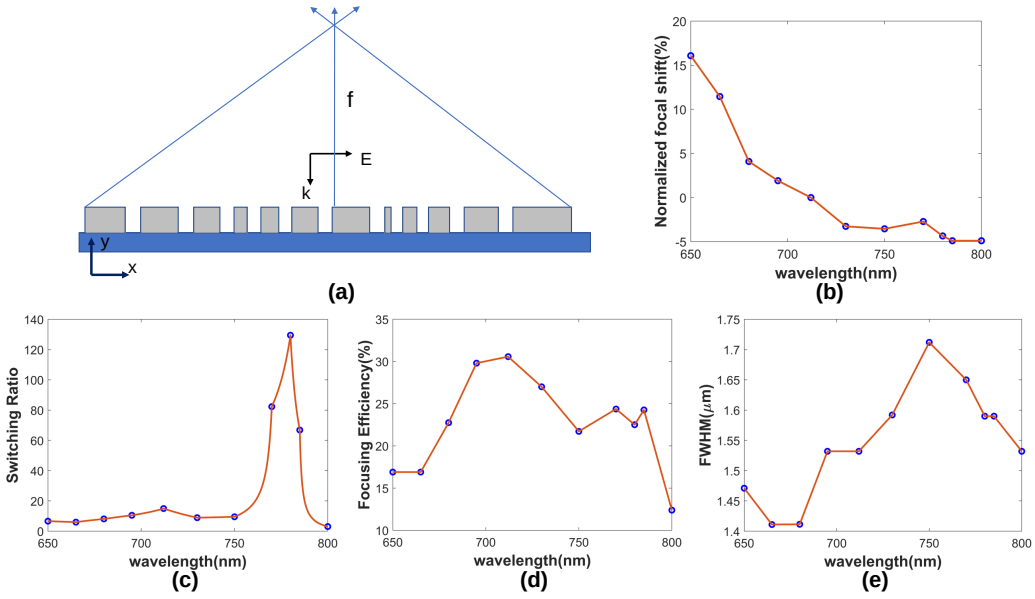

Fig. 7. **(a)** Schematic representation of the designed metasurface for a focal length of f, **(b)** Focal length shift normalized to the reference wavelength at 712nm in the on state, **(c)** Intensity switching ratio at the on and off states, **(d)** Focusing efficiency, **(e)** Full-width at half-maximum(FWHM) of the broadband system as a function of wavelength in the on state. The lines joining the simulation data points have been added for ease of visualization.

The achromatic focusing of the multifunctional meta-device in the on state is quantified by

normalized focal shift and is defined as $(f(\lambda) - f_0)/f_0$. $f(\lambda)$ and f_0 represent the focal lengths at a wavelength λ and at the reference wavelength of 712nm respectively. This value remains between ±5% over the range of 678-795nm and within ±4% in our designed band of 685.6nm to 774nm as depicted in Fig. 7(b).

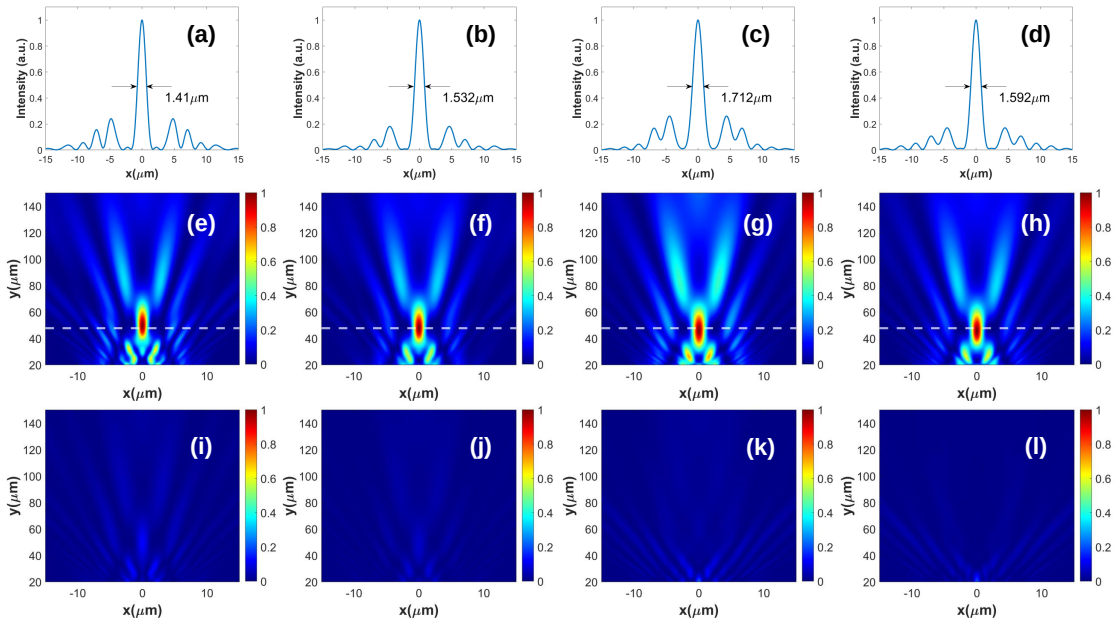

Fig. 8. Focusing and switching characteristics of the designed metalens. **(a-d)** Normalized cross-sectional intensity profile. The x-y plane spatial field profiles for the **(e-h)** insulating (on state) and **(i-l)** metallic (off state) phase of VO_2 at four different frequencies. The four operating wavelengths are 680nm, 712nm, 750nm, and 780nm moving from left to right. The color bars in each wavelength have been normalized by the corresponding on-state field maxima. The white dashed lines represent the focal plane at the reference wavelength (712nm) and illustrate the small shift in focal length over the operating bandwidth.

The switching ability is evaluated by switching ratio, which is the ratio of squared maximum intensities in the on and off states. This quantity remains above 8 throughout the design band with a maximum value of 129.5 (Fig. 7(c)), proving an excellent switching characteristic of our meta-device in the visible regime. Fig. 8 illustrates the spatial field distributions in the on and off state for four different wavelengths in our design regime. The distributions clearly show the contrast in the on-off states. The small shifts from the reference focal plane (white dashed lines) in Fig.8(e-h) represent the achromatic focusing in the on state.

Fig. 7(d) depicts the FWHM of our metalens over the range of 650nm to 800nm. The values are in very good agreement with the theoretical limit ($\frac{0.514\lambda}{NA}$), showing the diffraction-limited focusing performance of the device in on state [54]. The focusing efficiency is shown in Fig. 7(e). This value is defined as the ratio of power in a circle with a radius of $1.5 \times$ FWHM around the on-axis focal point and the incident power in the on state [55]. The efficiency remains between 22-30.57% over the designed frequency range but drops sharply beyond that. This low efficiency may be attributed to the relatively high absorption at some points, even in the on state. Table 1 compares our designed structure and other relevant metasurfaces. Our switching ratio (21.1dB) is the highest among all the broadband metalens-absorber devices. The other performance

Table 1. Comparison of our switchable metalens structure with previously reported metalens-absorber platforms.

Switching mechanism	**Operating wavelength range**	**Switching ratio**	**Focusing efficiency**	**Focal shift**	**Reference**
Polarization switching	632,670,710, 750nm	12dB	–	Focal plane switching with wavelength	[32]
PCM(GST)	1.49-1.65μm	16	23-33%	13.6%	[37]
PCM(GSST)	5.2μm	29.5dB	23.7%	–	[53]
PCM(VO_2)	10-11.2μm	25	26.3-48.4%	14.38%	[38]
PCM(GST)	10-11μm	–	–	10.92%	[39]
PCM(VO_2)	678-795nm	129.5 (21.1dB)	19.1-30.57%	9.48%	**This work**

parameters are also in excellent agreement with the previously reported ones. The only related device in the visible range [32] is not achromatic and is polarization-switched, further asserting the novelty of our proposed platform.

The excellent broadband switching and focusing characteristic of our designed metasurface quantified by the switching ratio and focal shift and visually shown in Fig. 8 makes it suitable for applications like optical switches for integrated photonics, communication networks, and imaging [56]. As a specific application, the switchable metalens can be used in bio-imaging as a focusing element with protective features against an overdose of illumination. VO_2 in our device can be switched optically, even by a laser with a high dose. The red region of the visible spectrum is generally preferred for imaging due to its ability to penetrate deeper into the bio-tissues [57]. Nearly constant focal length over a broadband regime in the red portion shows the suitability of our device for imaging in the on state. The high switching ratio under red light illumination means that it can automatically turn off under overdose protecting the tissue samples. This novel structure can pave the way for future smart miniaturized imaging systems in the visible regime.

6. Conclusion

In this article, we report a reconfigurable multifunctional broadband metasurface in the visible range. The device can be switched between an achromatic metalens and a nearly perfect absorber by changing the VO_2 from insulating to the metallic state through optical, thermal, or electrical stimulus. The low contrast in optical properties between PCM states at visible wavelengths has been a major obstacle to reconfigurable multifunctional broadband device development in the past. The cascaded meta-atom of our metasurface allowed us to overcome this obstacle. Multiple FP cavities formed at the metallic state of VO_2 ensured nearly perfect absorption for the off state

and reasonable transmission in the on state for the 689.3nm to 774.6nm spectral band, showing excellent switching behavior. We used this absorber cell to construct our final meta-device. We have performed numerical simulations to verify the achromatic focusing and broadband switching characteristics of the metasurface. Analysis of the spatial field profiles for the on and off states reveals a maximum intensity contrast of 21.1dB and a focal length shift of 9.48% in the on state over the wavelength range of 678-795nm. This is the highest reported switching ratio for a broadband metalens-absorber platform in any frequency band. These features make our device suitable as an optical switch in many applications. We expect the findings of our work to pave the way for novel reconfigurable multifunctional devices in the visible range for complex miniaturized photonic platforms.

Disclosures. The authors declare no conflict of interest.

Data Availability Statement. Data underlying the findings of this work are not public at this time but will be made available upon reasonable request to the authors.

References

1. C. L. Holloway, A. Dienstfrey, E. F. Kuester, J. F. O'Hara, A. K. Azad, and A. J. Taylor, "A discussion on the interpretation and characterization of metafilms/metasurfaces: The two-dimensional equivalent of metamaterials," Metamaterials **3**, 100–112 (2009).
2. D. Chen, X. Sun, S. Wang, Y. Qi, S. Wang, and J. Wang, "Design of dielectric deflecting metasurface and metalens in the visible-light range," Opt. engineering **60**, 035104–035104 (2021).
3. Q. Lou and Z. N. Chen, "Sidelobe suppression of metalens antenna by amplitude and phase controllable metasurfaces," IEEE Trans. on Antennas Propag. **69**, 6977–6981 (2021).
4. G. M. Akselrod, J. Huang, T. B. Hoang, P. T. Bowen, L. Su, D. R. Smith, and M. H. Mikkelsen, "Large-area metasurface perfect absorbers from visible to near-infrared," Adv. Mater. **27**, 8028–8034 (2015).
5. R. Bilal, M. Baqir, P. Choudhury, M. Naveed, M. Ali, and A. Rahim, "Ultrathin broadband metasurface-based absorber comprised of tungsten nanowires," Results Phys. **19**, 103471 (2020).
6. Y. Yang, H. Wang, F. Yu, Z. Xu, and H. Chen, "A metasurface carpet cloak for electromagnetic, acoustic and water waves," Sci. reports **6**, 20219 (2016).
7. Z. Wei, Y. Cao, X. Su, Z. Gong, Y. Long, and H. Li, "Highly efficient beam steering with a transparent metasurface," Opt. express **21**, 10739–10745 (2013).
8. W. Yang, G. Qu, F. Lai, Y. Liu, Z. Ji, Y. Xu, Q. Song, J. Han, and S. Xiao, "Dynamic bifunctional metasurfaces for holography and color display," Adv. Mater. **33**, 2101258 (2021).
9. C. Shen, R. Xu, J. Sun, Z. Wang, and S. Wei, "Metasurface-based holographic display with all-dielectric meta-axilens," IEEE Photonics J. **13**, 1–5 (2021).
10. H. Zhang, X. Sha, Q. Chen, J. Cheng, Z. Ji, Q. Song, S. Yu, and S. Xiao, "All-dielectric metasurface-enabled multiple vortex emissions," Adv. Mater. **34**, 2109255 (2022).
11. J. Li, Y. Chen, Y. Hu, H. Duan, and N. Liu, "Magnesium-based metasurfaces for dual-function switching between dynamic holography and dynamic color display," ACS nano **14**, 7892–7898 (2020).
12. F. Ding, S. Zhong, and S. I. Bozhevolnyi, "Vanadium dioxide integrated metasurfaces with switchable functionalities at terahertz frequencies," Adv. Opt. Mater. **6**, 1701204 (2018).
13. G. K. Shirmanesh, R. Sokhoyan, P. C. Wu, and H. A. Atwater, "Electro-optically tunable multifunctional metasurfaces," ACS nano **14**, 6912–6920 (2020).
14. L. Cong, P. Pitchappa, Y. Wu, L. Ke, C. Lee, N. Singh, H. Yang, and R. Singh, "Active multifunctional microelectromechanical system metadevices: applications in polarization control, wavefront deflection, and holograms," Adv. Opt. Mater. **5**, 1600716 (2017).
15. H. Yang, X. Cao, F. Yang, J. Gao, S. Xu, M. Li, X. Chen, Y. Zhao, Y. Zheng, and S. Li, "A programmable metasurface with dynamic polarization, scattering and focusing control," Sci. reports **6**, 1–11 (2016).
16. X. Gao, H. C. Zhang, L. W. Wu, Z. X. Wang, P. H. He, Z. Gao, and T. J. Cui, "Programmable multifunctional device based on spoof surface plasmon polaritons," IEEE Trans. on Antennas Propag. **68**, 3770–3779 (2020).
17. W. Bai, P. Yang, S. Wang, J. Huang, D. Chen, Z. Zhang, J. Yang, and B. Xu, "Actively tunable metalens array based on patterned phase change materials," Appl. Sci. **9**, 4927 (2019).
18. N. Raeis-Hosseini and J. Rho, "Metasurfaces based on phase-change material as a reconfigurable platform for multifunctional devices," Materials **10**, 1046 (2017).
19. T. Cao and M. Cen, "Fundamentals and applications of chalcogenide phase-change material photonics," Adv. theory simulations **2**, 1900094 (2019).
20. F. Ding, Y. Yang, and S. I. Bozhevolnyi, "Dynamic metasurfaces using phase-change chalcogenides," Adv. Opt. Mater. **7**, 1801709 (2019).
21. K. Wilson, C. Marocico, and A. Bradley, "Dynamic structural colour using vanadium dioxide thin films," J. Phys. D: Appl. Phys. **51**, 255101 (2018).

22. A. Crunteanu, M. Fabert, J. Cornette, M. Colas, J.-C. Orlianges, A. Bessaudou, and F. Cosset, "Electric field-assisted metal insulator transition in vanadium dioxide (vo2) thin films: optical switching behavior and anomalous far-infrared emissivity variation," in *Oxide-based Materials and Devices VI,* vol. 9364 (SPIE, 2015), pp. 42–52.
23. A. Cavalleri, T. Dekorsy, H. H. Chong, J.-C. Kieffer, and R. W. Schoenlein, "Evidence for a structurally-driven insulator-to-metal transition in vo 2: A view from the ultrafast timescale," Phys. Rev. B **70**, 161102 (2004).
24. H. Kocer, S. Butun, B. Banar, K. Wang, S. Tongay, J. Wu, and K. Aydin, "Thermal tuning of infrared resonant absorbers based on hybrid gold-vo2 nanostructures," Appl. Phys. Lett. **106**, 161104 (2015).
25. M. J. Dicken, K. Aydin, I. M. Pryce, L. A. Sweatlock, E. M. Boyd, S. Walavalkar, J. Ma, and H. A. Atwater, "Frequency tunable near-infrared metamaterials based on vo 2 phase transition," Opt. express **17**, 18330–18339 (2009).
26. T. Badloe, I. Kim, and J. Rho, "Moth-eye shaped on-demand broadband and switchable perfect absorbers based on vanadium dioxide," Sci. Reports **10**, 4522 (2020).
27. Y. Zhao, Q. Huang, H. Cai, X. Lin, and Y. Lu, "A broadband and switchable vo2-based perfect absorber at the thz frequency," Opt. communications **426**, 443–449 (2018).
28. Y. Zhang, L. Shi, D. Hu, S. Chen, S. Xie, Y. Lu, Y. Cao, Z. Zhu, L. Jin, B.-O. Guan *et al.*, "Full-visible multifunctional aluminium metasurfaces by in situ anisotropic thermoplasmonic laser printing," Nanoscale Horizons **4**, 601–609 (2019).
29. M. Liu, W. Zhu, P. Huo, L. Feng, M. Song, C. Zhang, L. Chen, H. J. Lezec, Y. Lu, A. Agrawal *et al.*, "Multifunctional metasurfaces enabled by simultaneous and independent control of phase and amplitude for orthogonal polarization states," Light. Sci. & Appl. **10**, 107 (2021).
30. F. Cheng, L. Ding, L. Qiu, D. Nikolov, A. Bauer, J. P. Rolland, and A. N. Vamivakas, "Polarization-switchable holograms based on efficient, broadband multifunctional metasurfaces in the visible regime," Opt. Express **26**, 30678–30688 (2018).
31. Q. Dai, Z. Guan, S. Chang, L. Deng, J. Tao, Z. Li, Z. Li, S. Yu, G. Zheng, and S. Zhang, "A single-celled tri-functional metasurface enabled with triple manipulations of light," Adv. Funct. Mater. **30**, 2003990 (2020).
32. D. Wintz, P. Genevet, A. Ambrosio, A. Woolf, and F. Capasso, "Holographic metalens for switchable focusing of surface plasmons," Nano letters **15**, 3585–3589 (2015).
33. P. Zhou, G. Zheng, F. Xian, and L. Xu, "Dynamically switchable polarization-independent and broadband metasurface perfect absorber in the visible and near-infrared spectra regime," Results Phys. **11**, 278–282 (2018).
34. K. V. Sreekanth, S. Han, and R. Singh, "Ge2sb2te5-based tunable perfect absorber cavity with phase singularity at visible frequencies," Adv. Mater. **30**, 1706696 (2018).
35. J. He, M. Zhang, S. Shu, Y. Yan, and M. Wang, "Vo 2 based dynamic tunable absorber and its application in switchable control and real-time color display in the visible region," Opt. Express **28**, 37590–37599 (2020).
36. Z. Wang, P. Zhou, and G. Zheng, "Electrically switchable highly efficient epsilon-near-zero metasurfaces absorber with broadband response," Results Phys. **14**, 102376 (2019).
37. W. Bai, P. Yang, J. Huang, D. Chen, J. Zhang, Z. Zhang, J. Yang, and B. Xu, "Near-infrared tunable metalens based on phase change material ge2sb2te5," Sci. reports **9**, 5368 (2019).
38. W. Chen, R. Chen, Y. Zhou, and Y. Ma, "A switchable metasurface between meta-lens and absorber," IEEE Photonics Technol. Lett. **31**, 1187–1190 (2019).
39. X. Ma, R. Song, Z. Fan, and S. Zhou, "Phase-change metasurface by u-shaped atoms for photonic switch with high contrast ratio," Coatings **11**, 1499 (2021).
40. T.-A. Pham, T.-K. Nguyen, R. K. Vadivelu, T. Dinh, A. Qamar, S. Yadav, Y. Yamauchi, J. A. Rogers, N.-T. Nguyen, and H.-P. Phan, "A versatile sacrificial layer for transfer printing of wide bandgap materials for implantable and stretchable bioelectronics," Adv. Funct. Mater. **30**, 2004655 (2020).
41. X. Cheng, Q. Gao, K. Li, Z. Liu, Q. Liu, Q. Liu, Y. Zhang, and B. Li, "Enhanced phase transition properties of vo2 thin films on 6h-sic (0001) substrate prepared by pulsed laser deposition," Nanomaterials **9**, 1061 (2019).
42. L. Liao, Z. Chen, X. Xu, G. Chen, R. Yao, R. Zhou, L. Zhong, Y. Mao, and M. Yang, "Effects of oxidation curing and sintering temperature on the microstructure formation and heat transfer performance of freestanding polymer-derived sic films for high-power leds," Ceram. Int. **44**, 6072–6080 (2018).
43. N. A. Abu Hatab, J. M. Oran, and M. J. Sepaniak, "Surface-enhanced raman spectroscopy substrates created via electron beam lithography and nanotransfer printing," ACS nano **2**, 377–385 (2008).
44. E. D. Palik, *Handbook of optical constants of solids*, vol. 3 (Academic press, 1998).
45. S. Wang, M. Zhan, G. Wang, H. Xuan, W. Zhang, C. Liu, C. Xu, Y. Liu, Z. Wei, and X. Chen, "4h-sic: a new nonlinear material for midinfrared lasers," Laser & Photonics Rev. **7**, 831–838 (2013).
46. M. Shabani and A. Mir, "Design and analysis of an ultra-broadband polarization-independent wide-angle plasmonic thz absorber," IEEE J. Quantum Electron. **57**, 1–8 (2021).
47. M. A. Bavil, L. Gao, and X. Sun, "A compact nanoplasmonics filter and intersection structure based on utilizing a slot cavity and a fabry–perot resonator," Plasmonics **8**, 631–636 (2013).
48. C.-P. Huang and C.-T. Chan, "Deep subwavelength fabry-perot resonances," EPJ Appl. Metamaterials **1**, 2 (2014).
49. W. T. Chen, A. Y. Zhu, V. Sanjeev, M. Khorasaninejad, Z. Shi, E. Lee, and F. Capasso, "A broadband achromatic metalens for focusing and imaging in the visible," Nat. nanotechnology **13**, 220–226 (2018).
50. W. T. Chen, A. Y. Zhu, J. Sisler, Z. Bharwani, and F. Capasso, "A broadband achromatic polarization-insensitive metalens consisting of anisotropic nanostructures," Nat. communications **10**, 355 (2019).

51. Q. Cheng, M. Ma, D. Yu, Z. Shen, J. Xie, J. Wang, N. Xu, H. Guo, W. Hu, S. Wang *et al.*, "Broadband achromatic metalens in terahertz regime," Sci. Bull. **64**, 1525–1531 (2019).
52. F. Balli, M. A. Sultan, A. Ozdemir, and J. T. Hastings, "An ultrabroadband 3d achromatic metalens," Nanophotonics **10**, 1259–1264 (2021).
53. M. Y. Shalaginov, S. An, Y. Zhang, F. Yang, P. Su, V. Liberman, J. B. Chou, C. M. Roberts, M. Kang, C. Rios *et al.*, "Reconfigurable all-dielectric metalens with diffraction-limited performance," Nat. communications **12**, 1225 (2021).
54. F. Balli, M. Sultan, S. K. Lami, and J. T. Hastings, "A hybrid achromatic metalens," Nat. communications **11**, 3892 (2020).
55. S. Banerji, M. Meem, A. Majumder, F. G. Vasquez, B. Sensale-Rodriguez, and R. Menon, "Imaging with flat optics: metalenses or diffractive lenses?" Optica **6**, 805–810 (2019).
56. Z. T. Xie, J. Wu, H. Fu, and Q. Li, "Tunable electro-and all-optical switch based on epsilon-near-zero metasurface," IEEE Photonics J. **12**, 1–10 (2020).
57. W. Yin, L. Zhao, L. Zhou, Z. Gu, X. Liu, G. Tian, S. Jin, L. Yan, W. Ren, G. Xing *et al.*, "Enhanced red emission from gdf3: Yb3+, er3+ upconversion nanocrystals by li+ doping and their application for bioimaging," Chem. Eur. J. **18**, 9239–9245 (2012).